

# Three-dimensional isometric tensor networks

Maurits Tepaske\* and David J. Luitz†

Max Planck Institute for the Physics of Complex Systems, Noethnitzer Str. 38, 01167 Dresden, Germany

(Dated: December 25, 2021)

Tensor network states are expected to be good representations of a large class of interesting quantum many-body wave functions. In higher dimensions, their utility is however severely limited by the difficulty of contracting the tensor network, an operation needed to calculate quantum expectation values. Here we introduce a method for time evolution of three-dimensional isometric tensor networks which respects the isometric structure and therefore renders contraction simple through a special canonical form. Our method involves a tetrahedral site splitting which allows to move the orthogonality center of an embedded tree tensor network in a simple cubic lattice to any position.

Using imaginary time evolution to find an isometric tensor network representation of the ground state of the 3D transverse field Ising model across the entire phase diagram, we perform a systematic benchmark study of this method in comparison with exact Lanczos and quantum Monte Carlo results. We show that the obtained energy matches the exact groundstate result accurately deep in the ferromagnetic and polarized phase, while the regime close to the critical point requires larger bond dimensions. This behavior is in close analogy with the two dimensional case, which we also discuss for comparison.

## I. INTRODUCTION

The Hilbert space dimension of many-body systems grows exponentially with the number of constituents, making the direct handling of many-body wavefunctions impractical for large systems. Tensor networks are an attempt to “tame” the many-body wavefunction, by expressing it in terms of local tensors, which are contracted according to the network structure. This reduces the complexity from an exponential to a polynomial number of variables. While in principle any wavefunction can be expressed as a tensor network, some particularly entangled states require exponentially large local tensors (i.e. the virtual dimension  $D$  of any of the tensor axes becomes large). Fortunately, the manifold of wavefunctions expressible with finite  $D$  tensor networks includes in particular wavefunctions with area law entanglement, which are expected to be relevant for the description of groundstates of many local quantum many-body systems [1–3].

Tensor network states are particularly successful in one dimension (1D), where they are known as “matrix-product states” (MPS) [4], which have become state-of-the-art machinery for the classical simulation of 1D many-body systems. This popularity rests primarily on the existence of powerful algorithms to variationally optimize the energy of the state (e.g. the density matrix renormalization group (DMRG)) [5] as well as on the ability to compute wavefunction overlaps  $\langle \phi | \psi \rangle$  and matrix elements of local operators  $\langle \phi | \hat{O} | \psi \rangle$  both exactly and efficiently. In particular the second property does not generalize to the higher-dimensional variants of MPS known as “projected-entangled pair states” (PEPS)

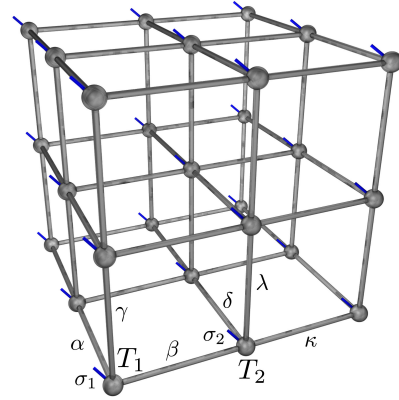


FIG. 1. A generic 3D PEPS ansatz for the cubic lattice, where the tensors  $T_{i\alpha\beta\gamma\delta\kappa\lambda}^{\sigma_i}$  are represented by spheres. The blue legs denote the physical degrees of freedom  $\sigma_i$  and the gray legs denote the virtual degrees of freedom. The connections depict contractions between the virtual legs of neighboring tensors.

[6]. It turns out that the exact calculation of a matrix element of an operator  $\hat{O}$  in an arbitrary PEPS state  $\langle \text{PEPS} | \hat{O} | \text{PEPS} \rangle$  – requiring the full contraction of the resulting tensor network – is generally inefficient for generic finite PEPS with open boundary conditions (OBC) already in two dimensions [6–10]. While PEPS are readily formulated in three dimensions (cf. Fig. 1), currently no efficient contraction method is known.

Therefore, even though PEPS are efficient representations of area law entangled quantum many-body wavefunctions, it is often difficult to extract useful information from them. The central problem for the generalization of powerful 1D methods to higher dimensions is caused by the fact that cutting a bond in a higher-dimensional PEPS does not separate the network into two disconnected pieces, in contrast to 1D MPS. In MPS methods, the separation of the network into unique “left” and

\* mtepaske@pks.mpg.de

† dluitz@pks.mpg.de

“right” parts by cutting any bond is exploited using an orthonormal basis to represent the left/right states and one can decimate the basis to the dominant components by truncating to the largest singular values [11] in an optimal way. This property is the foundation of MPS evolution algorithms [12]. The absence of separability in higher-dimensional PEPS diminishes the effectiveness of purely local evolution algorithms, where in the case of a nearest-neighbor interacting system the tensor network is optimized by iterating over the bonds and applying a two-site gate to each bond followed by a truncation of this bond according to the standard time evolving block decimation (TEBD) [4, 11]. Instead, optimal truncation and hence optimal evolution requires each gate to be accompanied by a contraction of the full network (dubbed “full update”) instead of just two tensors, which leads to an enormous computational cost [8].

One way around the inefficiency of full contraction is to instead perform the contraction approximately [6, 8–10], sacrificing precision for speed. Recently there appeared multiple works [13–16] which suggest an attractive alternative: to construct finite PEPS in an *explicit canonical form* in which it can be contracted both exactly and efficiently in a way that local truncation again becomes optimal just like for MPS, thereby circumventing the mentioned problems that occur when dealing with generic PEPS. This does induce a loss of generality, restricting its subspace in Hilbert space to a subspace of generic PEPS, reducing the expressivity of the network [17]. While the effect of this restriction is not yet clear, it becomes irrelevant in the limit of large bond dimensions and therefore seems at least in principle controllable.

In [13] a class of finite 2D PEPS called “isometric tensor network states” (isoTNS) was introduced for which  $\langle \text{PEPS} | \text{PEPS} \rangle$  reduces to a canonical MPS norm, and which can be time-evolved using an efficient local evolution algorithm called TEBD<sup>2</sup>. Here we will generalize the isoTNS ansatz to 3D and develop a natural extension of TEBD<sup>2</sup> which we call TEBD<sup>3</sup>. This generalization is an important step forward towards the development of efficient techniques to simulate generic 3D quantum many-body systems for cases which are not accessible to quantum Monte Carlo methods due to a sign problem. This is particularly important due to the limited number of existing finite 3D PEPS algorithms [18, 19] and generic simulation methods for 3D quantum many-body systems in general [20–22].

## II. METHOD

A generic finite 3D PEPS ansatz for a 3D many-body spin-1/2 system can be written in the local basis  $\sigma_i = \pm 1$  as

$$|\text{PEPS}\rangle = \sum_{\sigma_1 \dots \sigma_N} \mathcal{C}(T_1^{\sigma_1} \dots T_N^{\sigma_N}) |\sigma_1 \dots \sigma_N\rangle, \quad (1)$$

where  $T_i^{\sigma_i}$  represents the set of tensors which contain the complex-valued variational parameters and which are spatially arranged like the spins  $\sigma_i$ . Here  $\mathcal{C}$  indicates that all tensors are contracted, giving complex scalar coefficients, which is usually done by choosing the amount of virtual degrees of freedom per  $T_i^{\sigma_i}$  equal to the lattice connectivity and then contracting nearest-neighbors. In Fig. 1 this is illustrated for a cubic lattice with open boundary conditions, where the pairs of virtual degrees of freedom are represented by the gray bonds and the physical (spin) degrees of freedom are represented by the blue free legs, i.e. in a particular basis we get the tensors  $T_{i\alpha\beta\gamma\delta\kappa\lambda}^{\sigma_i}$ .

In order to calculate  $\langle \text{PEPS} | \text{PEPS} \rangle$  we would contract this tensor network with the physical legs of its conjugate, which we would then have to contract down to a scalar.

### A. General properties of isoTNS

The goal of this work is to design a type of 3D tensor network that allows for the full network contraction to be done exactly and efficiently. To this end we impose an additional structure on the PEPS shown in Fig. 1, such that  $\langle \text{PEPS} | \text{PEPS} \rangle = \langle \text{MPS} | \text{MPS} \rangle$  becomes manifest. In particular, we choose the majority of the  $T_i$  to be isometric, meaning that these  $T_i$  reduce to identities when contracted with their conjugate over a subset of the legs, e.g.

$$\sum_{i\alpha\beta\gamma\delta\kappa} T_{\sigma_i}^{\dagger\alpha\beta\gamma\delta\kappa\lambda} T_{\sigma_i}^{\alpha\beta\gamma\delta\kappa\eta} = \mathbb{1}^{\lambda\eta}, \quad (2)$$

and

$$\sum_{i\alpha\beta\gamma\delta} T_{\sigma_i}^{\dagger\alpha\beta\gamma\delta\kappa\lambda} T_{\sigma_i}^{\alpha\beta\gamma\delta\nu\eta} = \mathbb{1}^{\kappa\nu} \mathbb{1}^{\lambda\eta}. \quad (3)$$

If  $T$  is unitary instead of isometric, these constraints also hold under  $T \rightarrow T^\dagger$ , which in the case of an isometry instead gives a projector.

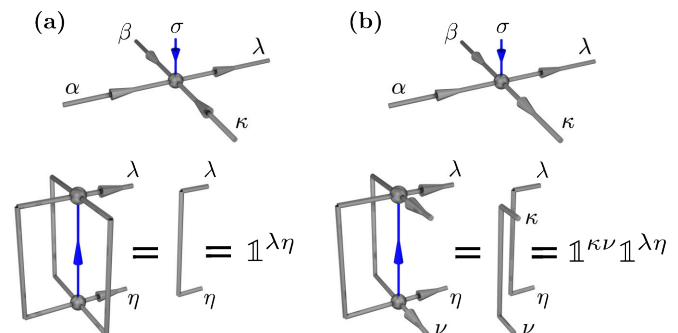


FIG. 2. The isometry constraints are encoded by decorating the tensor legs with arrows (top row). Here panel (a) corresponds to Eq. 2 and panel (b) to Eq. 3, where in the bottom figures the tensor shown in the top panel is contracted with its conjugate to yield identities.

In the language of tensor network diagrammatics we can represent these constraints by decorating the legs with arrows [4, 13], where incoming arrows represent contracted indices in the isometry constraint and where outgoing arrows represent free indices. In Fig. 2 we illustrate this notation for tensors with four virtual legs. Here the diagrams in the upper panels encode the isometry constraints depicted in the lower panels. Specifically, Fig. 2a corresponds to Eq. 2 and Fig. 2b to Eq. 3. Note that for convenience we choose a single arrow direction after contracting the legs. In the same spirit we will omit the arrows on physical legs from here on, since we will always choose these to be incoming.

Using these isometric tensors we can construct tensor networks that identically reduce to a single pair of tensors (the orthogonality center) upon contraction with its conjugate, which are called isoTNS [13]. In Fig. 3 we show a few snapshots of this reduction for a two-dimensional isoTNS on a  $3 \times 3$  square lattice. Before employing the isometry constraints we have the network depicted in Fig. 3a. Here we allow the red and gray legs to have distinct bond dimensions  $\chi$  and  $D$ , which is based on the observation that for the chosen pattern of arrows we can first reduce the network to a canonicalized MPS amplitude, as shown in Fig. 3b.

The distinction between red MPS bonds and gray non-MPS bonds is an important aspect of the isoTNS ansatz, as it will allow us to increase the accuracy of correlators while increasing the bond dimension on only a small part of the tensor network. In the benchmarking section we will see that in some situations the accuracy is indeed greatly increased when we increase  $\chi$  while keeping  $D$  constant. This is especially favorable because we will also see that the computational cost of the time-evolution algorithm scales much more favorably in  $\chi$  than in  $D$ .

Due to the remaining isometry structure we can further reduce the MPS amplitude down to a single site, as shown in Fig. 3c. This final site, which is called the "orthogonality center" and which is colored red in Fig. 3, therefore fully encodes the norm, just like the orthogonality center of MPS in 1D [4]. It also encodes the one-body correlators of that site, but if we want to calculate its two-body correlator with another site we can already no longer reduce the network to a single site. In terms of the arrow language this reduction requires that the arrows flow towards the MPS and within the MPS towards the orthogonality center, which can be characterized as having only incoming arrows.

For example, say we want to calculate a local two-body correlator involving the nearest-neighbors of the orthogonality center in Fig. 3. In this case the MPS reduction that yields Fig. 3c from Fig. 3b would be halted at the operators, since there we can no longer utilize the isometry relations from Fig. 2, which consequently also holds for the sites that follow these operators in the stream of arrows. Hence we would be left with a MPS correlator instead of a single-site correlator, the accuracy of which is controlled by  $\chi$ . We illustrate this for a local two-body

correlator  $\langle \text{isoTNS} | O_1 O_2 | \text{isoTNS} \rangle$  in Fig. 4. Here it is important that the center lies between the operators in order to take full advantage of the isometry structure.

Clearly this MPS calculation is more expensive than the single-site calculation, but crucially it still scales polynomially in its bond dimensions and size [4]. When we instead consider local correlators with one or more operators located outside of the MPS, the isometry reductions yield a genuine 2D network, which would have to be contracted in order to get the correlator. As a result the correlator can no longer be computed efficiently, illustrating the importance of being able to move the embedded MPS through the network. We will address this in the next section.

It should be noted that by calculating correlators as MPS correlators we do reduce the formal expressibility of the ansatz, as compared to generic PEPS, since it is well known that MPS with finite  $\chi$  can only encode exponentially decaying correlations [4] whereas generic PEPS can also encode algebraic correlations [23]. This means that the isoTNS ansatz can only encode exponential correlations. Nonetheless, for finite systems the bond dimension can always be chosen large enough to encode algebraic correlations which are cut off by the system size.

Before discussing the time-evolution algorithm, which we will do directly for the 3D isoTNS, we first consider how Fig. 3 generalizes to 3D. The principles that underlie the isometry reduction property generalize trivially to 3D. As in 2D, we design the network for optimal contraction properties, which means that we introduce an embedded low dimensional network, to which all arrows flow, avoiding any loops of arrows. It turns out that the minimal suitable embedded structure is now a tree tensor network (TTN) [24], and in particular a TTN with the geometry of a star [25], where all branches are connected to the orthogonality center, to which all arrows flow (it should be noted that in 2D the embedded string is actually also a TTN when the orthogonality center is in the bulk). This situation is displayed in Fig. 5, where we illustrate how a particular 3D isoTNS configuration would reduce upon contraction with its conjugate.

## B. Evolving 3D isoTNS

We will now explain how the TTN is moved through the 3D isoTNS during its trotterized time-evolution, specializing to nearest-neighbor interacting Hamiltonians. As discussed, in order to take full advantage of the isoTNS representation we can apply two-body time evolution gates when both sites occupy the TTN and one of the sites is at the orthogonality center. We will find that this gives rise to a threefold-nested TEBD, which we call TEBD<sup>3</sup> in analogy to TEBD<sup>2</sup> for 2D isoTNS.

The evolution will take place slice-wise, starting from the vertical slice of the cube in Fig. 5a that contains two TTN strands, which is shown separately in Fig 6a. In each slice, only bonds along the TTN branch (vertical in

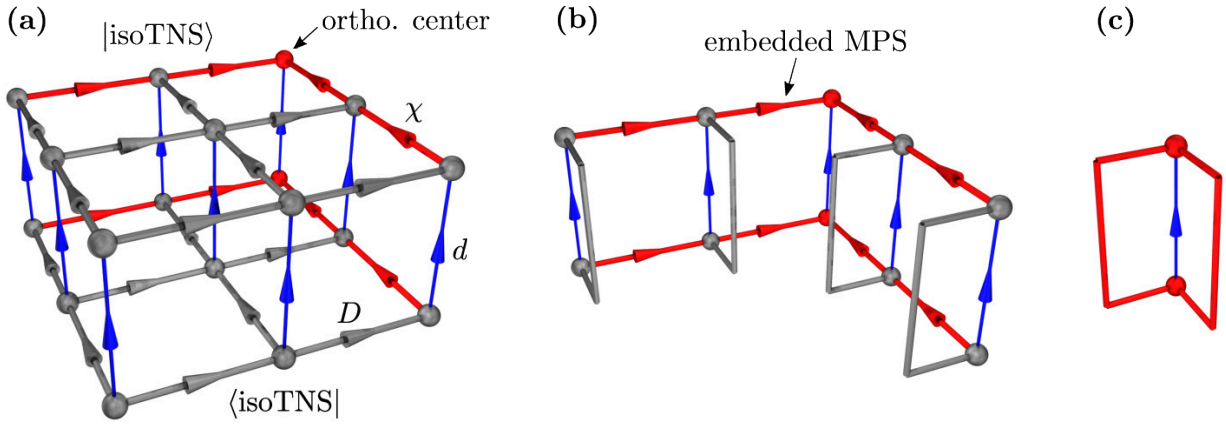


FIG. 3. Multiple stages of the reduction of  $\langle \text{isoTNS} | \text{isoTNS} \rangle$  to a contraction of just two tensors, illustrated for a 2D isoTNS on a  $3 \times 3$  square lattice. Panel (a) shows the amplitude before employing the isometry constraints, where the gray bonds have dimension  $D$ , the red bonds have dimension  $\chi$ , and the blue bonds have dimension  $d$ . Panel (b) shows the canonical (classical, since it has no external legs) MPS that is obtained after utilizing a large part of the isometry structure, motivating the distinction between gray and red bonds. Note that the gray legs which stem from the reduction effectively enlarge the local Hilbert space of the MPS. Panel (c) shows the final pair of contracted tensors that remains after fully utilizing the isometry structure.

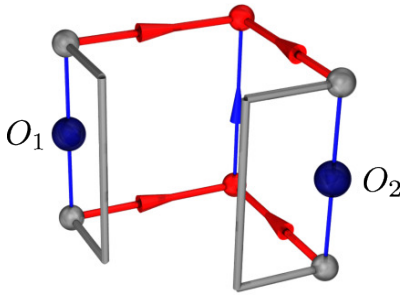


FIG. 4. The final product of the isometry reductions when calculating the local two-body correlator  $\langle \text{isoTNS} | O_1 O_2 | \text{isoTNS} \rangle$ , leaving us with a MPS correlator that has to be fully computed.

the slice shown in Fig. 8, we will call them “columns” in each slice) are evolved. To evolve this slice using two-body gates we first trotterize the imaginary time-evolution operator  $\exp(-d\tau H)$ , which is for an imaginary time-step of size  $d\tau$ , as

$$e^{-d\tau H} \approx \prod_{s_x} e^{-d\tau H_{s_x}} \prod_{s_y} e^{-d\tau H_{s_y}} \prod_{s_z} e^{-d\tau H_{s_z}}, \quad (4)$$

where  $s_i \in \{1, \dots, L\}$  with  $i \in \{x, y, z\}$  labels all slices of the cube.  $H_{s_x}$  contains only terms of bonds which are part of a “column” in the slice parallel to the  $y-z$  plane and going through  $s_x$ , similarly for  $H_{s_y}$  and  $H_{s_z}$ . This way, all bonds are evolved. Since we will be dealing exclusively with nearest-neighbor interacting systems, these terms are further Trotter decomposed to contain only two

site gates

$$e^{-d\tau H_{s_x}} \approx \prod_{b_i} e^{-d\tau h_{b_i}}, \quad (5)$$

where  $b_i$  labels all bonds corresponding to “columns” in slice  $s_x$ , and  $h_{b_i} \in \mathbb{C}^{4 \times 4}$  represents the two site Hamiltonian of the bond  $b_i$ .

### 1. Evolving the columns of a slice

To begin the evolution we apply a two-site gate at the initial orthogonality center, as illustrated in Fig. 6b. For clarity we omit the transverse legs in most of the panels, only restoring them when crucial for the interpretation. After contracting the gate with the involved pair of tensors we split them again, using a truncated singular value decomposition (SVD), in a way that the orthogonality center is moved downwards by one site, as illustrated in Fig. 6c. Concretely, we reshape the contraction as a matrix  $A$  and perform a truncated SVD  $A \approx U s V^\dagger$ , after which we take  $U$  as the upper tensor and  $s V^\dagger$  as the lower tensor (they become isometries after reshaping back). In Fig. 7 we show this operation in terms of network diagrammatics, where the dark gray color indicates that the leg is formed by combining multiple gray legs.

It should be noted that this operation requires that the contracted pair of tensors forms the orthogonality center, meaning that one of the tensors has to occupy the orthogonality center, in which case the truncation is automatically optimal. Consequently a column can only be evolved when all of its transverse legs have incoming arrows, as is the case for the TTN column in Fig. 6a. In

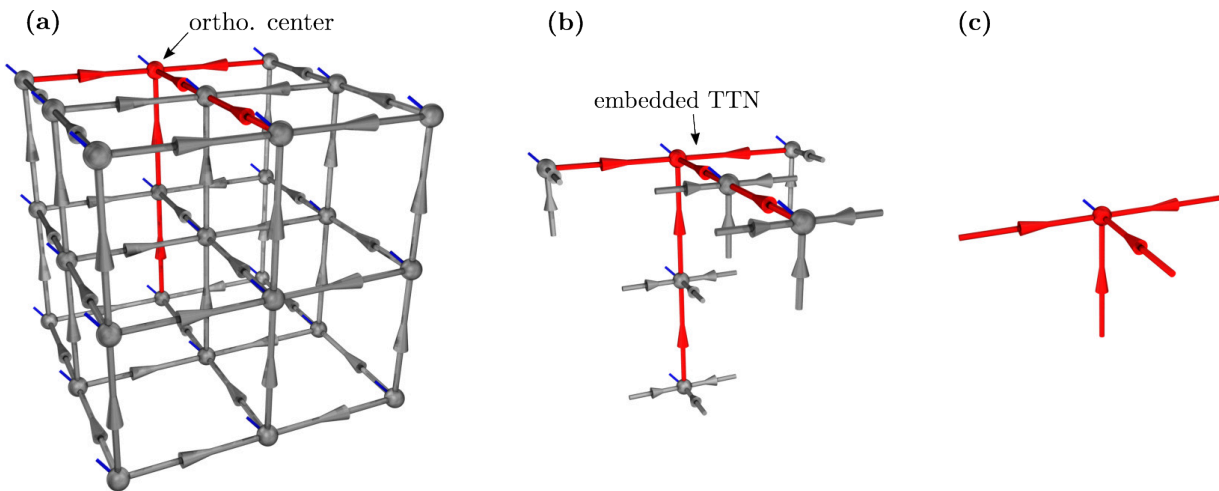


FIG. 5. The reduction of a particular 3D isoTNS configuration as it would occur upon contraction with its conjugate. In panel (a) we show the initial network. In panel (b) we show the canonical TTN that would remain after utilizing most of the isometry structure. In panel (c) we show how the canonical TTN further reduces to a single site, i.e. the orthogonality center.

the coming sections we will see that the SVD maneuver from Fig. 7 is involved in every part of TEBD<sup>3</sup>.

Having applied the first gate and subsequently moved the orthogonality center downwards by one site, we now repeat these steps at the new orthogonality center, after which we end up at the bottom of the column. This is illustrated in Fig. 6d. Now in order to evolve the next column we have to transfer the TTN strand to the next column. To achieve this we use the column-splitting procedure introduced in [13], which is constituted by a sequence of "triangle-splittings" at the orthogonality center. In Fig. 8 we illustrate a triangle-splitting of the orthogonality center in Fig. 6d, which is shown separately in 8a. By performing two truncated SVDs on the center, where the amount of truncation is chosen according to the color coding and where the direction of the SVDs is dictated by the isometry structure, we get the decomposition shown in Fig 8b. Because the triangle-splitting is simply a sequence of SVDs it can only be executed at the orthogonality center.

It should be noted that the upper and bottom-right tensors produced in Fig. 8b have only virtual legs, which is required as they will be absorbed in tensors which already have a physical leg. In particular, we see in Fig. 8c that the upper tensor gets absorbed upwards immediately after the splitting, thereby shifting the orthogonality center upwards by one site to yield the configuration shown in Fig. 6e. The bottom-right tensor will get absorbed rightwards, but only after having split each tensor in the column. To repeat the triangle-splitting on the new center from Fig. 6e we temporarily combine its tilted legs with its horizontal legs as designated in Fig. 8c, after which we again get the picture in Fig. 8c. After repeating the triangle-splitting and restoring the combined legs we obtain the network configuration shown in Fig. 6f.

Having reached the uppermost tensor of the column we now finalize the column-splitting by first combining the legs as in Fig. 8c and subsequently performing a single truncated SVD instead of the triangle-splitting. This results in the configuration shown in Fig. 6g, where we restored the transverse legs to emphasize that the virtual column does not have transverse legs.

Finally we absorb the new virtual TTN strand into the neighboring column of isometries, after which we have successfully moved the TTN strand to the next column and modified the isometry structure accordingly, as shown in Fig. 6h. Note that this absorption increases the bond dimension of the TTN strand from  $\chi$  to  $D\chi$ , which will be truncated back to  $\chi$  during its evolution.

To improve the quality of the triangle-splitting we insert a pair of unitary "disentangler"  $U^\dagger U = \mathbb{1}$  across the red bond in the triangle [13]. The legs between the disentanglers have the same direction as those outside, as can be seen in Fig. 8c where the disentanglers have been absorbed into the connected tensors. To decrease the information loss due to the second truncated SVD in the triangle-splitting, which is used to create the red triangle bond, we optimize the disentanglers by iteratively minimizing the second Rényi entropy across this bond [26], which we will call  $|B\rangle$  for the following.

The Rényi entropy across  $|B\rangle$  is formulated in terms of its density matrix

$$\rho_B = \text{tr}(U|B\rangle\langle B|U^\dagger), \quad (6)$$

where we trace out all legs of one tensor while leaving the other tensor untouched. We will use the second Rényi entropy

$$S_2 = -\ln \text{tr}(\rho_B^2), \quad (7)$$

for which there exists a convex iterative optimization algorithm [26]. This entropy reduction is performed in or-

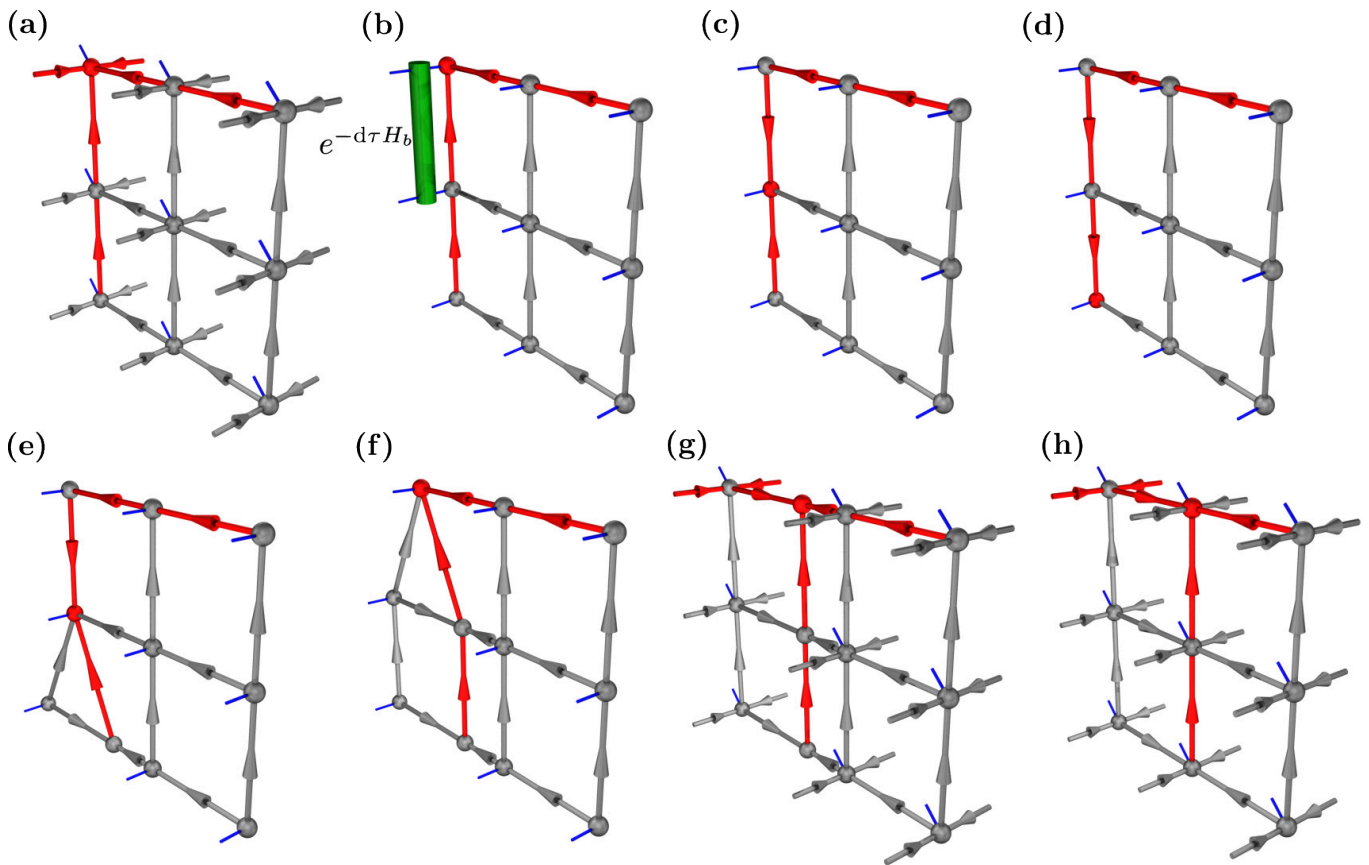


FIG. 6. The evolution of a slice in the 3D isoTNS, where for clarity we omit the transverse legs in most of the panels. In panel (a) we show the initial slice, which is the middle slice from Fig. 5. In panel (b) we apply a two-body gate at the orthogonality center, after which in panel (c) we perform a truncated SVD that shifts the orthogonality center downwards. In panel (d) we repeat this after which the orthogonality center is at the bottom of the first column. In panel (e) we perform the triangle-splitting from Fig. 8 on the orthogonality center, which we repeat in panel (f) after combining the tilted bonds as indicated in Fig. 8c. Now that we have reached the top of the column we again combine the tilted bonds at the new orthogonality center and subsequently perform a truncated SVD, after which we have transferred the TTN strand to a temporary column that has only virtual legs, as shown in panel (g) where we restored the transverse legs to emphasize that the virtual column has no transverse legs. By absorbing the virtual column into the neighboring isometry column, yielding the configuration in panel (g), we have finally moved the TTN strand to the middle column. The increased bond dimensions  $D_\chi$  are truncated back to  $\chi$  when evolving the new column. Repeating the column-splitting and subsequently the column-evolution once more we have evolved all columns in the slice.



FIG. 7. The graphical representation of a truncated SVD of the reshaped orthogonality center, which yields an isometry  $U$  and a new orthogonality center  $sV^\dagger$ . This can be used to move the orthogonality center through a 1D subset with only incoming external arrows.

der to increase the weight of the  $\chi$  largest singular values in the red triangle bond, thereby reducing the information loss due to the truncation.

After repeating the steps in Fig. 6 on the new middle column we have moved the TTN strand from the first to

the last column while evolving all but the last column. To finalize the slice-evolution we evolve the last column via the usual procedure, giving us the network shown in Fig. 10a, for which the middle slice's columns have now been evolved.

## 2. Splitting a slice

Having evolved the columns in the first slice we now want to transfer the two TTN strands to the next slice and repeat. To achieve this we use a tetrahedron-splitting on the orthogonality center, which is illustrated in Fig. 9a.

Concretely, by performing three truncated SVDs on

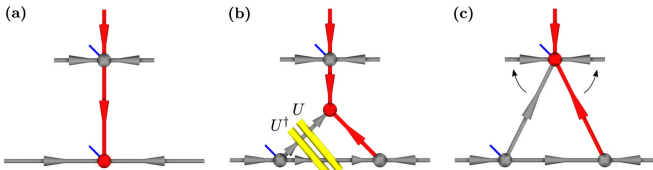


FIG. 8. The triangle-splitting of the orthogonality center that is used multiple times in succession to shift a TTN strand to a neighboring column. By performing two truncated SVDs we split the orthogonality center shown in panel (a) into the triangle shown in panel (b), where the upper tensor is the new orthogonality center and where the lower two tensors are isometries. Note that the top and bottom-right tensors have only virtual legs. The amount of truncation during the SVDs is based on the usual color coding, where we inserted a pair of disentanglers  $U^\dagger U = \mathbb{1}$  across the TTN bond, depicted as yellow cylinders, in order to increase the weight of the  $\chi$  remaining singular values. After the splitting we absorb the top tensor upwards, as shown in panel (c). To now perform the splitting from panel (b) on the new orthogonality center we first temporarily combine the tilted legs as indicated by the arrows, so that the orthogonality center again looks as in panel (a).

the center and suitably reshaping the resulting tensors we can get the splitting shown in Fig. 9b, where only one of the tetrahedron tensors has a physical leg. Due to the SVDs this tetrahedron-splitting can only be performed at the orthogonality center. As in the triangle-splitting we insert a pair of disentanglers in order to reduce the second Rényi entropy (7) across the red tetrahedron bond. The amount of truncation during the SVDs is again based on the color coding and their direction dictated by the displayed isometry structure.

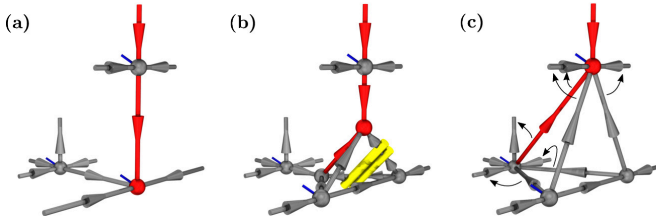


FIG. 9. The tetrahedron-splitting used in the procedure that transfers the two TTN strands in Fig. 10a to the next slice. In panel (a) we show the required initial tensor configuration, i.e. an orthogonality center. In panel (b) we show the tetrahedron that results from three consecutive SVDs, where the disentanglers across the TTN bond are again depicted as yellow cylinders. Note that only one of the four produced tensors has a physical leg. In panel (c) we have absorbed the top tensor upwards and the back tensor backwards. To repeat the tetrahedron-splitting on the new orthogonality center we temporarily combine the tilted legs as indicated by the arrows.

To continue the slice-splitting we then absorb the virtual top tensor upwards and the virtual back tensor back-

wards, leaving the remaining virtual tensor to be absorbed only after having split each tensor in the slice. This is illustrated at the tensor level in Fig. 9c and at the network level in Fig. 10b. To repeat the tetrahedron-splitting on the new orthogonality center we temporarily combine its upwards-tilted legs with its horizontal legs, as indicated by the upper three arrows in Fig. 9c, so that the orthogonality center again looks as in Fig. 9a. After performing the splitting and restoring the tilted legs, which have now become vertical legs, we get the network shown in Fig. 10c. Here we permanently combined the new red vertical bond with the gray vertical bond as shown in Fig. 9c, yielding a TTN bond with dimension  $D\chi$ .

Now that the orthogonality center is located at the top of the column we finally perform the triangle-splitting from Fig. 8, giving us the network shown in Fig. 10d. Here we can see that the vertical TTN strand has been moved by one column in the slice and that in the process we created a virtual column. Before repeating this 3D column-splitting on the new TTN strand we move the orthogonality center from the top to the bottom using SVDs, during which we truncate the enlarged vertical bonds back to  $D$ , and we temporarily combine the tilted legs in 10d with the horizontal legs as designated by the arrows in Fig. 9c. After this reshaping the orthogonality center again looks as in 9a, so that we can repeat the column-splitting. Doing this we have transferred the TTN strand to the final column in the slice.

We complete the slice-splitting by performing the 2D column-splitting from Fig. 7e-7h on this final column, resulting in the configuration shown in Fig. 10e. The newly created slice, which has only virtual legs and contains the two TTN strands, is then absorbed into the next slice, after which the strands have been successfully transferred as illustrated in Fig. 10f. Just like for the 2D column-splitting from Fig. 6 this absorption increases the bond dimensions of the new slice. These will be truncated back down to  $\chi$  or  $D$  during the evolution of the new slice.

### 3. Evolving the full network

With the machinery developed in the previous sections we can now perform a trotterized time-evolution where all truncation occurs at the orthogonality center, so that we obtain a local time-evolution that is globally optimal. We will illustrate this by considering the details of a single  $\text{TEBD}^3$  iteration, starting from the network in Fig. 11a.

We evolve the columns of the first slice, following the procedure depicted in Fig. 6, and subsequently move the TTN strands to the neighboring slice by utilizing the slice-splitting of Fig. 10. Repeating these steps for the middle slice we end up with the TTN strands in the last slice, where we evolve the final set of columns by using the slice-evolution of Fig. 6. We then use the column-splitting from Fig. 7e-7h to move the orthogonality cen-

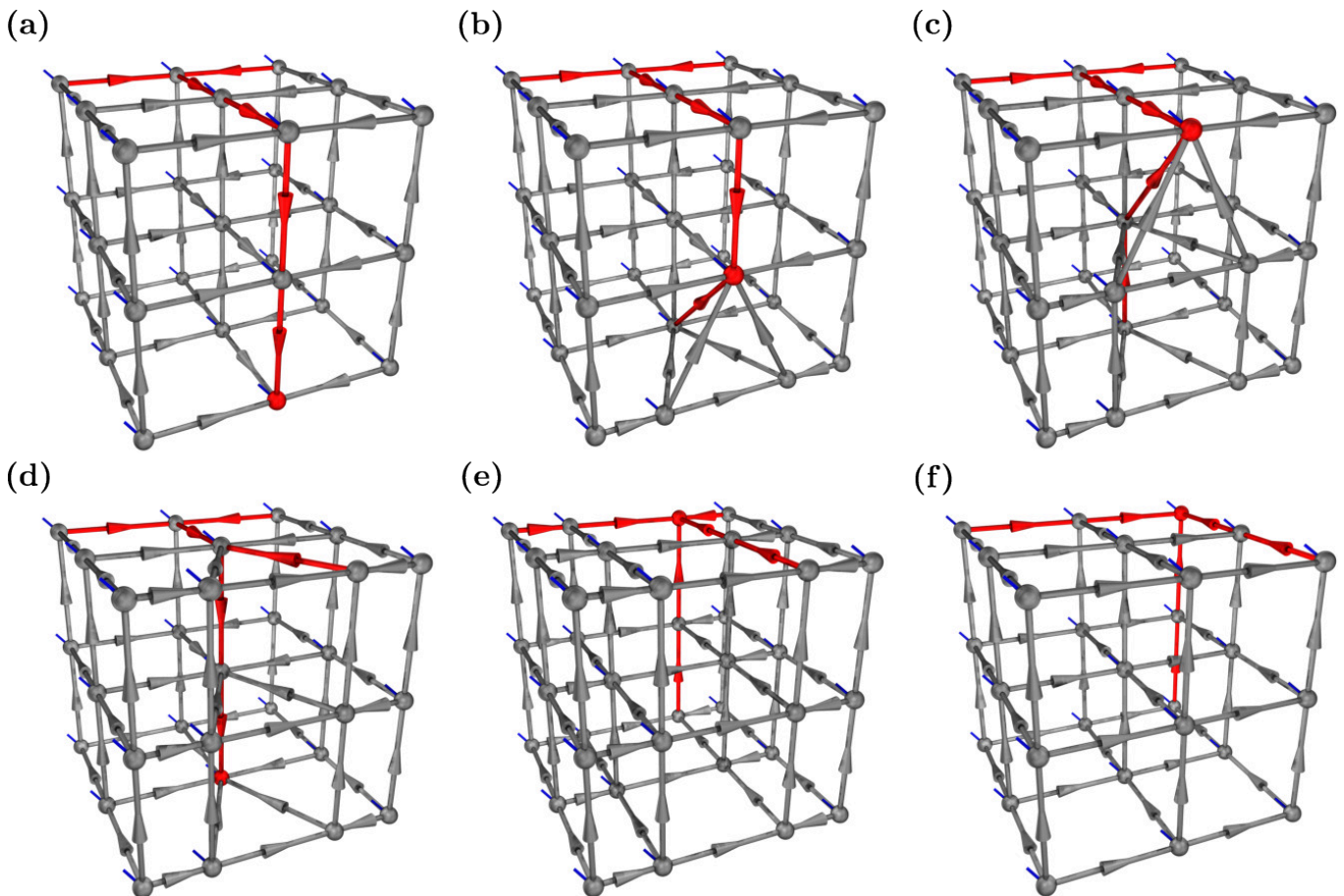


FIG. 10. The slice-splitting procedure by which we transfer the two TTN strands to the next slice after evolving the vertical bonds of a slice. In panel (a) we show the initial network, which is obtained from Fig. 5 by evolving the middle slice as shown in Fig. 6. In panel (b) we show the first step of the slice-splitting, where we employ the tetrahedron-splitting from Fig. 9 on the orthogonality center, thereby moving it upwards by one site. After temporarily combining the tilted legs with the horizontal legs as indicated by the arrows in Fig. 9c we repeat the tetrahedron-splitting on the new orthogonality center, which after restoring the legs yields panel (c). Now that the orthogonality center is located at the top of the column we again temporarily combine the tilted legs, but this time we apply the triangle-splitting from Fig. 8. We then move the orthogonality center from the top to the bottom of the column, resulting in the network shown in panel (d). We repeat this combination of evolving and column-splitting until we reach the final column, which is instead split via the procedure described in panels (e)-(h) of Fig. 6, yielding the network in panel (e). To finalize the transfer we absorb the new slice into the neighboring slice, resulting in the network shown in panel (f), where the increased bond dimensions will be truncated upon evolving the new slice's columns.

ter to its diagonally-opposite tensor in the slice, yielding the network shown in Fig. 11b for which all columns have now been evolved (as indicated by the green isometry bonds and dark-green TTN bonds).

To evolve the remaining two-thirds of the bonds we need to maneuver the final configuration from Fig. 11b to the initial configuration from Fig. 11a in a way that the new columns consist of non-evolved bonds. One such maneuver is a 90 degree rotation around the axis along 1-2 in Fig. 11b, which yields the network in Fig. 11c. For convenience we have numbered the corners in Fig. 11, so that the used maneuvers become obvious.

After performing the rotation we repeat the evolution of columns, giving us the network shown in 11d for which

two-thirds of the bonds have now been evolved. Finally, we maneuver the network such that the remaining third of non-evolved bonds become the new columns. We do this by first rotating with 90 degrees around the 2-3 axis in Fig. 11a and subsequently with 180 degrees around the 2-6 axis in Fig. 11a, giving us the network in 11e. We again evolve all the columns, resulting in Fig. 11f for which all bonds have now been evolved.

To complete the single iteration of TEBD<sup>3</sup> we maneuver the network in Fig. 11f back to the initial configuration in Fig. 11a. We do this by first rotating with 90 degrees around the 2-3 axis in Fig. 11a, then rotating with 90 degrees around the 1-2 axis in Fig. 11a, and finally reflecting in the 1-2 direction (i.e. sending 1 to 2

etc.). It should be noted that the order of slices is reversed with respect to the initial configuration, as can be seen from the labeling in Fig. 10.

#### 4. Expected performance

Now that we have developed the theoretical framework of TEBD<sup>3</sup> we can try to form some expectations on its behavior, such as how isoTNS with different  $(\chi, D)$  are expected to perform relative to each other. We base these predictions on the two main sources of error that enter TEBD<sup>3</sup>: the error due to the multitude of truncated SVDs and the error due to the trotterization. As noted in [13] these errors conspire in TEBD<sup>2</sup> to yield an energy-minimum in  $d\tau$ -space, which we consider in more detail in Appendix VI, where we will also discuss the case of TEBD<sup>3</sup>. For the current analysis we only need the truncation error, since we expect this to dictate the relation between the accuracy of TEBD<sup>3</sup> and its  $(D, \chi)$ .

To illustrate this relation we consider a simple tensor operation, where we contract two neighboring sites inside a single TTN strand and then perform a truncated SVD in order to regain the contracted red bond. This requires us to SVD a  $\chi D^4 \times \chi D^4$  matrix, yielding  $\chi D^4$  singular values, which we then truncate back down to  $\chi$ . This means that  $\chi(D^4 - 1)$  singular values are dropped, which scales quartically in  $D$  and linearly in  $\chi$ , indicating that by increasing  $D$  we are forced to omit a lot more singular values than when increasing  $\chi$ .

Since most of the weight should be concentrated in the first few singular values, this increased omission will likely not significantly alter the precision when  $\chi$  is large. If  $\chi$  is not large to this extent, the accuracy cannot be improved by increasing  $D$  and instead will likely deteriorate. Analogously, at some point a further increase in  $\chi$  will no longer improve the accuracy, since nearly all weight will already be included in the  $\chi$  largest singular values. On the other hand, since the first SVD in the triangle- and tetrahedral-splittings is used to generate gray bonds, as can be seen in Figs. 8 and 9, it can be expected that the column- and slice-splittings become more accurate when increasing  $D$ . We expect that the interplay between these effects gives rise to a crossover in the accuracy of various  $(D, \chi)$  configurations, i.e. only above a particular  $\chi$  it becomes favorable to use high  $D$  and for insufficient  $\chi$  it performs better with small  $D$ . We confirm these expectations later when analyzing our benchmark results.

#### 5. Computational complexity

Let us now examine the computational efficiency (i.e. time complexity) of TEBD<sup>3</sup> in terms of the bond dimensions  $\chi$  and  $D$ . At first sight there appear to be multiple candidates for the most costly operation, all involving a SVD. One sensible possibility seems to be the first SVD

in the tetrahedron-splitting from Fig. 9, although there also occur many costly SVDs when evolving the columns of a slice right after absorbing the virtual slice, in which case the bonds have grown as  $\chi \rightarrow \chi^2$  and  $d \rightarrow \chi d$ .

For example, when we have just absorbed the virtual slice and the network looks as in Fig. 5b, the first gate application is followed by the SVD of a  $d\chi^3 D \times d\chi D^5$  matrix. Here  $d$  denotes the dimension of the physical leg, i.e.  $d = 2$  for the spin-1/2 systems considered in this work. Since the computational efficiency of the SVD of a  $n \times m$  matrix is  $\mathcal{O}(\min(mn^2, m^2n))$  [27] we find that the computational efficiency of the mentioned SVD is  $\mathcal{O}(\min(d^3\chi^5 D^{11}, d^3\chi^7 D^7))$ . Similar but slightly different costs are obtained when the orthogonality center occupies e.g. a face of the cube or its bulk. When it occupies a face we have to SVD a  $d\chi^3 D^5 \times d\chi D^7$  matrix, yielding a cost of  $\mathcal{O}(\min(d^3\chi^5 D^{19}, d^3\chi^7 D^{17}))$ , and when it occupies the bulk we have to SVD a  $d\chi D^6 \times d\chi D^7$  matrix, yielding a cost of  $\mathcal{O}(d^3\chi^3 D^{19})$ .

Coming back to the tetrahedron-splitting, we note that the first SVD is especially costly when the tetrahedron-splitting is performed on a center with the maximal amount of combined legs, i.e. which has left, right and backwards pointing legs that have been combined with tilted legs as indicated by the arrows in Fig. 9c. The SVD is executed after combining the physical leg with the left-pointing virtual leg and combining the remaining legs, yielding a  $dD^3 \times \chi^2 D^4$  matrix and hence a cost of  $\mathcal{O}(d\chi^4 D^{11})$ . It is easy to see that the triangle-splitting from Fig. 8 has similar cost when it is used in a 3D setting.

By comparing the estimated costs we find that the largest contribution in  $\chi$  comes from the evolution of the orthogonality center when it occupies one of the faces, whereas the largest contribution in  $D$  is shared by the tetrahedron-splitting and the evolution of the orthogonality center when it occupies the bulk. We thus find that the computational efficiency of TEBD<sup>3</sup> is  $\mathcal{O}(\max(d^3\chi^5 D^{19}, d^3\chi^7 D^{17}))$ . This illustrates why it is wise from an efficiency standpoint to try improving on the accuracy by first increasing  $\chi$  before increasing  $D$ . Furthermore, because we perform the costliest operations roughly  $N = L^3$  times per iteration, we find that TEBD<sup>3</sup> scales linearly in  $N$ .

For completeness we note that similar considerations lead to a cost of  $\mathcal{O}(\max(d^3\chi^3 D^8, d^3\chi^4 D^6, d^3\chi^5 D^3))$  for TEBD<sup>2</sup>. This should be compared to the cost of  $\mathcal{O}(d^4\chi^2 D^4) + \mathcal{O}(d^2\chi^2 D^6) + \mathcal{O}(d^2\chi^3 D^4) + \mathcal{O}(d^6 D^6) + \mathcal{O}(\chi^2 D^8) + \mathcal{O}(\chi^3 D^4) + \mathcal{O}(d^3 D^{12})$  for the boundary MPS algorithm [10], where  $\chi$  now denotes the boundary MPS bond dimension and  $D$  the bulk tensor bond dimension (often at least  $\chi \propto D^2$  for convergence in  $\chi$  [10] although in practice this scaling is usually worse).

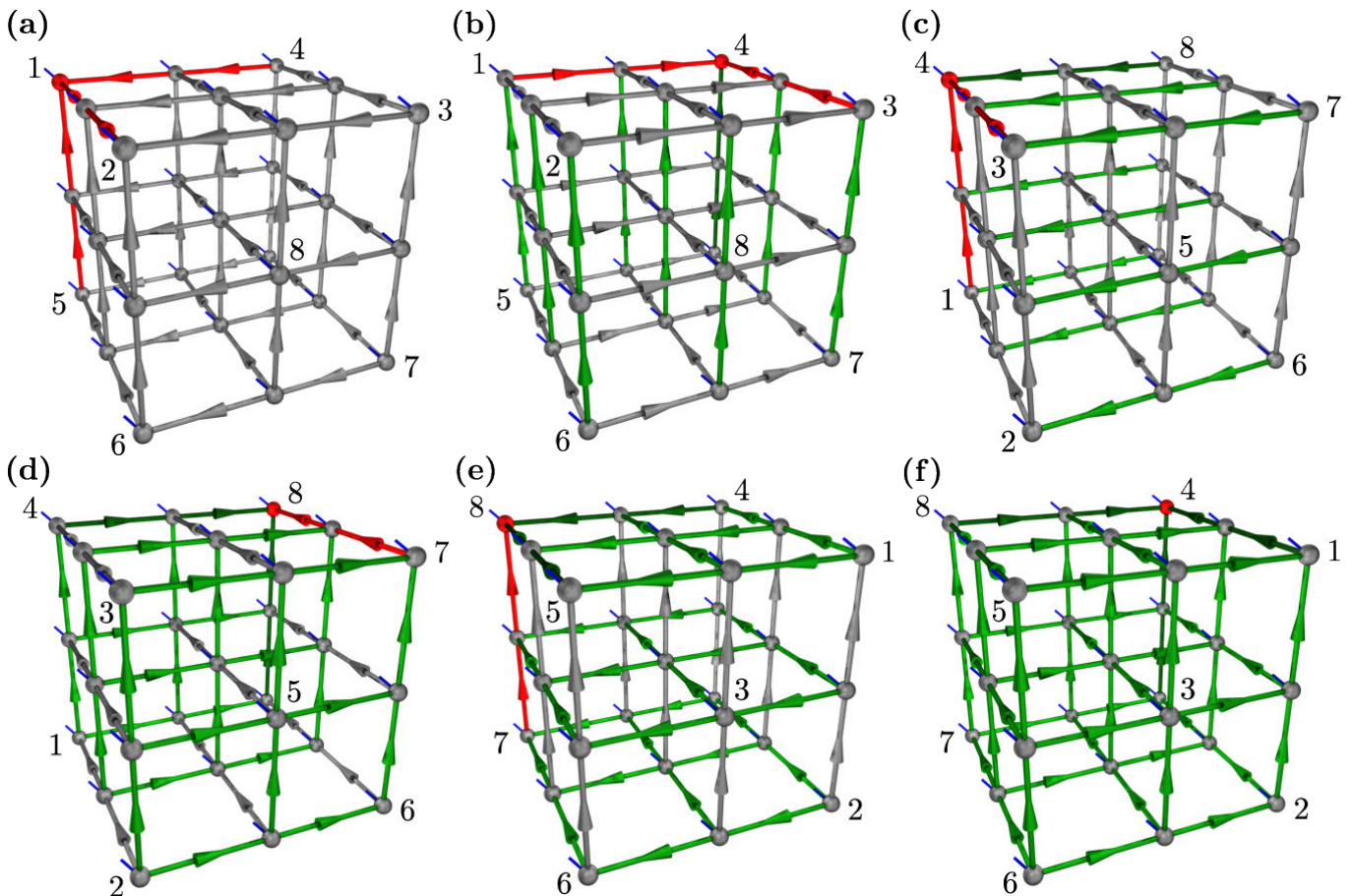


FIG. 11. A single iteration of the isoTNS evolution algorithm  $\text{TEBD}^3$ . Starting from the initial configuration in panel (a) we evolve all vertical bonds as described in the main text, yielding panel (b). Here the evolved isometry bonds have been colored green and the evolved TTN bonds have been colored dark-green. To evolve the next third of bonds we first rotate the network such that the TTN is again positioned as in panel (a), with the new columns consisting of un-evolved bonds, as displayed in panel (c). We then repeat the evolution of columns, yielding the network shown in panel (d) for which two-thirds of the bonds have now been evolved. To evolve the final third we again rotate the network such that the new columns consist of non-evolved bonds, yielding the network shown in panel (e). Finally, we repeat the evolution of columns, resulting in the network shown in panel (f), for which all bonds have now been evolved. After rotating this network back to the initial configuration in panel (a), in a way that the new columns are those which were evolved first, we have completed a single iteration of  $\text{TEBD}^3$ .

### III. BENCHMARKING

#### A. The benchmarking system

As a proof of principle we probe the accuracy of  $\text{TEBD}^3$  for imaginary time evolution to find an isoTNS approximation for the many-body groundstate of a simple 3D quantum many-body system: the ferromagnetic transverse-field Ising model (TFIM) on a cubic lattice with OBC:

$$H = - \sum_{\langle ij \rangle} \sigma_i^z \sigma_j^z - h \sum_i \sigma_i^x. \quad (8)$$

Here  $\vec{\sigma}_i \equiv (\sigma_i^x, \sigma_i^y, \sigma_i^z)$  corresponds to a spin-1/2 on site  $i$ , with  $\sigma^{x,y,z}$  the usual Pauli matrices, and the two-body sum runs over nearest-neighbor pairs  $(i, j)$ . Working in

the  $\sigma^z$ -basis, we see from eq. (8) that the TFIM Hamiltonian reduces to the (diagonal) classical limit if  $h \rightarrow 0$  and has a two fold degenerate ferromagnetic groundstate  $|\uparrow\uparrow\dots\uparrow\rangle$  and  $|\downarrow\downarrow\dots\downarrow\rangle$  in this case. Quantum fluctuations are generated by the uniform magnetic transverse (i.e. along the  $x$  direction) field of strength  $h$ . In the limit of strong fields  $h \rightarrow \infty$ , the ground state is unique and aligned with the field and a simple product state  $|\rightarrow\rightarrow\dots\rightarrow\rangle$  in the  $\sigma_x$  basis. Between these two limits, the competition between the  $x$  and  $z$  basis leads to a much more complex groundstate [28] and to a quantum phase transition as a function of  $h$  between the ferromagnetic phase (with spontaneous symmetry breaking of a discrete  $\mathbb{Z}_2$  spin flip symmetry) at  $h < h_c$  and the polarized phase at  $h > h_c$ . The value of the critical field on the 3D simple cubic lattice was numerically estimated to be  $h_c \approx 5.15813(6)$  [29].

Our main reason for choosing this model as a benchmark is its simplicity and the fact that it can be solved exactly using quantum Monte Carlo using the stochastic series expansion [30, 31]. The comparison to exact Monte Carlo results puts our benchmark on a solid footing.

Critical points are associated with a divergent correlation length and are therefore extremely challenging to study using tensor network methods. While the critical point becomes sharp only in the thermodynamic limit, a critical region is expected for finite systems. We generically expect our 3D isoTNS ansatz to be particularly challenged in this critical region, whereas its performance should be better deep in both phases since the ground-state in both phases is a “dressed” product state, which should be well representable by the isoTNS ansatz. We note that dealing with finite systems, in principle any state can be expected to be represented faithfully using large enough  $D$  and  $\chi$ .

We also note that we are using open boundary conditions, which induces a shift of the critical region towards small field values for small lattice sizes due to the relatively large ratio of one- to two-body couplings in the boundary terms.

Our two benchmark observables are the energy density  $\langle H \rangle / N$  and the  $x$ -magnetization density  $\sum_i \langle \sigma_i^x \rangle / N$ , which we compare to exact values in order to assess the accuracy of our isoTNS method. Moreover, for  $3 \times 3 \times 3$  we perform a more detailed analysis of the local contributions to the  $x$ -magnetization in Appendix VIB, where we also discuss the possibility of a bias arising from the sequential nature of our update (in space) of TEBD<sup>2</sup> and TEBD<sup>3</sup>.

## B. The benchmarking procedure

We perform imaginary time TEBD<sup>3</sup> propagation of the wave function represented by an isoTNS with bond dimensions  $(D, \chi)$  using the 3D TFIM Hamiltonian for a range of transverse fields  $h = 0.5, 1.0, 1.5, \dots, 8$  across the critical point and three system sizes  $L \times L \times L$  for  $L = 3, 4, 5$ . For the initial state, we take a simple product state  $|\psi_{\text{ini}}\rangle = |\uparrow\uparrow\uparrow \dots\rangle$ , polarized in the  $\sigma_z$  basis and evolve it in imaginary time until the results (in particular energy expectation value) are converged. This means, we perform the operation

$$|\psi_0\rangle \approx e^{-\beta \hat{H}} |\uparrow\uparrow\uparrow \dots \uparrow\rangle, \quad (9)$$

with using small timesteps  $d\tau$  and the Trotter decompositions explained in Sec. IIB, typically up to  $\beta \gtrsim 10$ .

We use a set of bond dimensions  $D = 2, 3$  and  $\chi = 4, 8, 12$ , which allows us to carefully analyze the convergence of our results towards the exact limit.

The exact reference values used for the energy density were obtained by the stochastic series expansion for which we used the ALPS library [32, 33]. Convergence to the ground state of these results was checked by a  $\beta$

doubling scheme. The Monte Carlo errors are negligible here and are of the order of the linewidth in our figures. For  $L = 3$ , we also performed Lanczos exact diagonalization, providing exact energy density and additionally the  $x$  magnetization of the ground state across the entire range of magnetic fields. In Appendix VIB we consider the local contributions to the  $x$  magnetization density in more detail, as part of a symmetry-analysis to determine a possible bias.

In order to provide a reference for the quality of our results, we furthermore performed TEBD<sup>2</sup> calculations for the 2D TFIM using the algorithm detailed in Ref. [13] for a comparable system size of  $5 \times 5$  lattice sites, for which exact Lanczos groundstate results can conveniently be obtained for comparison.

As mentioned in the method section of this work, both TEBD<sup>2</sup> and TEBD<sup>3</sup> have an energy minimum in  $d\tau$ -space, so for each  $(D, \chi, L, h)$  we will choose  $d\tau$  such that it approximately coincides with this minimum and use the corresponding isoTNS to calculate the  $x$ -magnetization. In Fig. 16 we show two TEBD<sup>3</sup> examples of the minimum in  $d\tau$ -space, for various  $(D, \chi)$  in the top panel and various system sizes in the bottom panel.

## C. Results

In this section, we present the results of our benchmarks for the 3D TFIM using TEBD<sup>3</sup> to evolve an initial ( $z$ -polarized) wavefunction in imaginary time to get an approximation of the groundstate.

Fig. 12 shows the calculation for the smallest system of  $3 \times 3 \times 3$  sites. The top panel of Fig. 12, shows the energy density  $E/N = \langle \hat{H} \rangle / N$  as a function of transverse field  $h$ . The colored crosses show the results for various bond dimensions  $(D, \chi)$ , while the red dashed line represents the exact groundstate energy density obtained by the Lanczos method. The overall agreement is good, although a discrepancy is visible at intermediate field strength of  $h \approx 3 \dots 5$ , in the finite size critical region. In order to analyze this discrepancy in more detail, we show the relative error in the inset, which clearly reveals high accuracy deep in both phases, and a peak in the error in the critical region.

From the data for  $D = 2$  (yellow through green) it is clear that it is initially useful to increase  $\chi$ , and the maximal relative error of the energy is reduced from 2.4% for  $\chi = 4$  to 1.8% for  $\chi = 8$ . However, a further increase of  $\chi$  from  $\chi = 8$  to  $\chi = 12$  shows a stagnation of the error, which can only be further reduced by increasing  $D$ . This supports the predictions made earlier in the method section. For  $D = 3$  we have likely not reached large enough  $\chi$  to observe this stagnation, instead showing significant improvement by going from  $\chi = 8$  with 1.6% maximum relative error to  $\chi = 12$  with 1.1%. Deep in the ferromagnetic and strong-field phases the error is much smaller than in the critical region, with 0.001% error at  $h = 0.5$  already for  $(D, \chi) = (2, 4)$  and the significantly larger

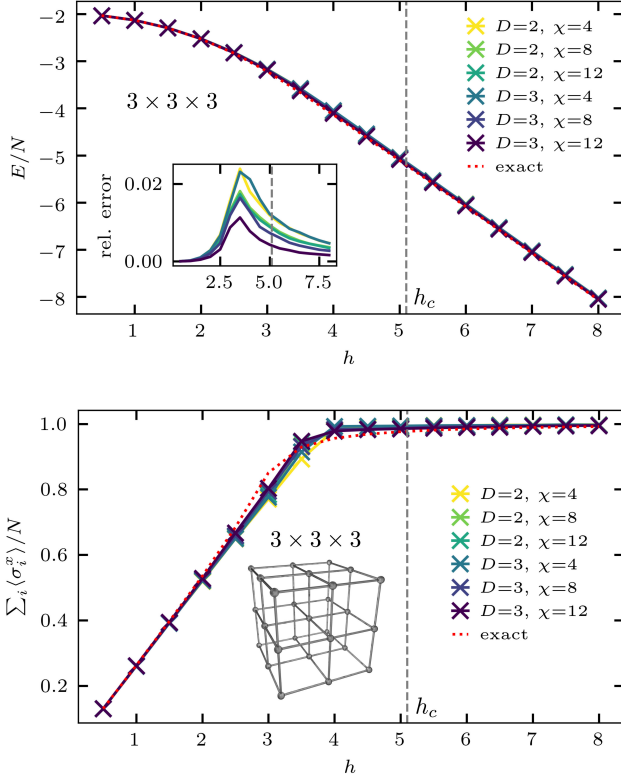


FIG. 12. **Top:** The energy density  $E/N$  and its accuracy relative to the exact value for the  $3 \times 3 \times 3$  cubic TFIM with OBC at various field strengths  $h$  across the critical point. Each curve belongs to a different set of bond dimensions  $(D, \chi)$ , and in the main plot we show the exact value with a red dotted line. **Bottom:** The x-magnetization  $\sum_i \langle \sigma_i^x \rangle / N$  for various field strengths around the critical point, for the same TFIM system as in the top panel.

0.47% at  $h = 8$ . While there is a discrepancy in precision for the low- and high-field regions, we see in Fig. 12 that increasing  $(D, \chi)$  leads to significant improvement at  $h = 8$ , whereas at  $h = 0.5$  we have less spectacular improvement. Specifically, with  $(D, \chi) = (3, 12)$  we get to 0.00081% at  $h = 0.5$  and to 0.16% at  $h = 8$ .

It should be noticed that  $(3, 4)$  is worse than  $(2, 4)$ , while  $(3, 8)$  is better than  $(2, 8)$ , which supports our prediction from the method section that there will be a crossover in accuracy. The bottom panel of Fig. 12 shows the analogous behavior for the x-magnetization density  $\sum_i \langle \sigma_i^x \rangle / N$  as a function of the field, again in comparison with the exact result (Lanczos, red dashed line). Deep in both phases, we get very accurate results, while in the critical regime there is a discrepancy, which decreases as the bond dimension is increased.

Next, we consider TEBD<sup>3</sup> for  $4 \times 4 \times 4$  in Fig. 13, where we see in the bottom panel that the behavior of the x-magnetization as a function of  $(D, \chi)$  is similar to that of  $3 \times 3 \times 3$ . The  $E/N$  behavior is also similar, although the

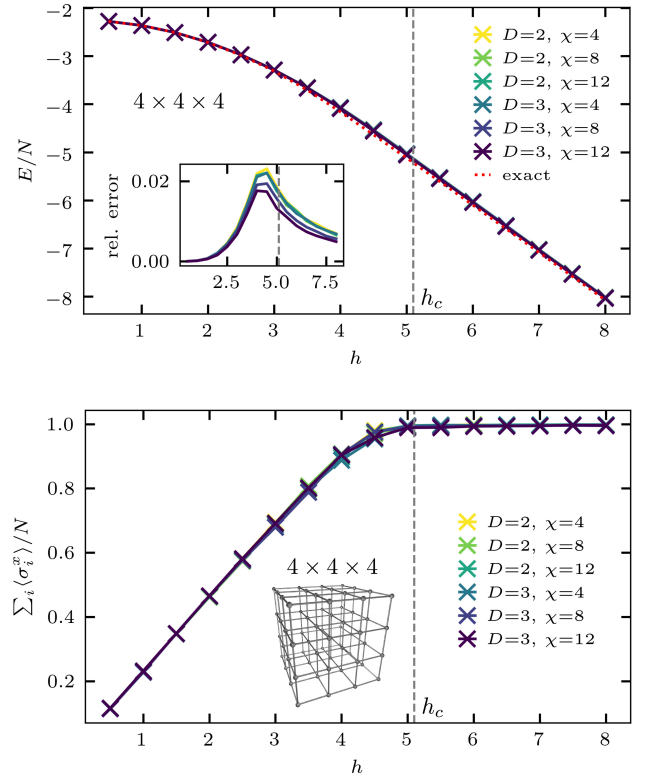


FIG. 13. **Top:** The energy density  $E/N$  and its accuracy relative to the exact value for the  $4 \times 4 \times 4$  cubic TFIM with OBC at various field strengths  $h$  across the critical point. Each curve belongs to a different set of bond dimensions  $(D, \chi)$ , and in the main plot we show the exact value with a red dotted line. **Bottom:** The x-magnetization  $\sum_i \langle \sigma_i^x \rangle / N$  for various field strengths around the critical point, for the same TFIM system as in the top panel.

accuracy and the increase in accuracy with larger  $(D, \chi)$  is slightly worse than for  $3 \times 3 \times 3$ . The best results for  $(D, \chi) = (3, 12)$  have a maximal relative error in the critical region of 1.8%, while in the ferromagnetic and strong-field phases we again get very accurate results. In particular, for  $(3, 12)$  we get a relative error of 0.000017% (which is of the order of our QMC error) at  $h = 0.5$  and 0.5% at  $h = 8.0$ .

We moreover see that the  $D = 2$  curves now accumulate faster as a function of  $\chi$ , whereas all  $D = 3$  curves still have significant gaps, and just like for  $3 \times 3 \times 3$  we observe the predicted crossover between  $D = 2$  and  $D = 3$ .

Finally, we consider TEBD<sup>3</sup> for  $5 \times 5 \times 5$  in Fig. 14, where we omitted the  $D = 3$  configurations due to the high computational cost. We see that the  $D = 2$  configurations behave similarly to those in Figs. 12 and 13, although the accumulation of curves as a function of  $\chi$  is even more rapid here. Specifically, there is barely any difference in accuracy for all field strengths, with the largest difference occurring at  $h = 4.5$  where the relative energy

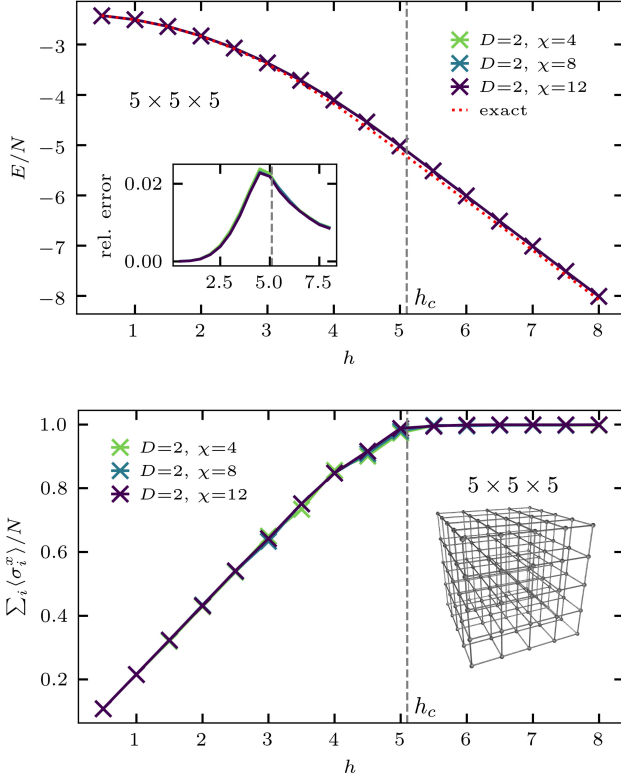


FIG. 14. **Top:** The energy density  $E/N$  and its accuracy relative to the exact value for the  $5 \times 5 \times 5$  cubic TFIM with OBC at various field strengths  $h$  across the critical point. Each curve belongs to a different set of bond dimensions  $(D, \chi)$ , and in the main plot we show the exact value with a red dotted line. **Bottom:** The x-magnetization  $\sum_i \langle \sigma_i^x \rangle / N$  for various field strengths around the critical point, for the same TFIM system as in the top panel.

error is 2.4% for  $(2, 4)$  and 2.3% for  $(2, 8)$  and  $(2, 12)$ . In the low- and high-field regions we again get much higher accuracy than in the critical region, with for  $(2, 12)$  now 0.00091% error at  $h = 0.5$  and 0.85% at  $h = 8.0$ . Here, the QMC values have an error of order  $10^{-5}$  for all  $h$ .

Overall, the comparison of our results across different system sizes reveals a very accurate representation of the ground state wavefunction deep in the ferromagnetic phase (with relative energy errors below 0.02% for  $h$  up to 1 on all system sizes and  $(D, \chi)$ ) even for the relatively small bond dimensions  $(D, \chi)$  which are reachable on current computers. The accuracy is slightly less good in the polarized phase, with a relative energy error below 0.3% from  $h = 5.5$  if we take the best  $3 \times 3 \times 3$  network, below 1.1% with the best  $4 \times 4 \times 4$  network, and below 1.8% with the best  $5 \times 5 \times 5$  network. The accuracy is worst in the critical regime, as expected, where the relative energy error does not drop below 1.1% for  $3 \times 3 \times 3$ , 1.8% for  $4 \times 4 \times 4$  and 2.3% for  $5 \times 5 \times 5$ . Here it should be remembered that the results for  $3 \times 3 \times 3$  and  $4 \times 4 \times 4$

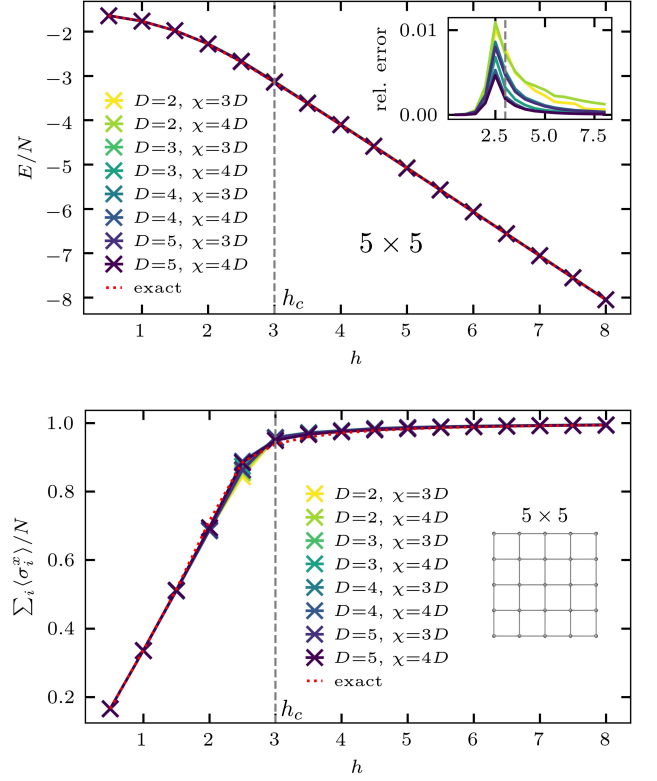


FIG. 15. **Top:** The energy density  $E/N$  and its accuracy relative to the exact value for the  $5 \times 5$  square TFIM with OBC at various field strengths  $h$  across the critical point. Each curve belongs to a different set of bond dimensions  $(D, \chi)$ , and in the main plot we show the exact value with a red dotted line. **Bottom:** The x-magnetization  $\sum_i \langle \sigma_i^x \rangle / N$  for various field strengths around the critical point, for the same TFIM system as in the top panel.

are obtained with maximal bond dimensions  $(3, 12)$  while for  $5 \times 5 \times 5$  the maximal bond dimension is  $(2, 12)$ .

We see a clear trend towards the exact result (both for the energy as well as for the  $x$ -magnetization) as the bond dimension is increased. At this stage, it is not clear whether a better accuracy for the same values of  $(D, \chi)$  can be achieved by a more sophisticated variational energy optimization.

In order to put the quality of these results into perspective, we perform the same benchmark for the two dimensional TFIM on the square lattice, using TEBD<sup>2</sup> for the imaginary time evolution according to the method described in Ref. [13] for a system of  $5 \times 5$  sites. It is clear that the simulation of a two dimensional system is much simpler than that of a three dimensional system and we therefore expect the isoTNS results to have a higher accuracy for the same choice of bond dimension. At this stage, it is not clear whether a better accuracy for the same values of  $(D, \chi)$  can be achieved by a more sophisticated variational energy optimization.

The bottom panel of Fig. 15 shows the energy density as a function of transverse field  $h$  in the  $5 \times 5$  TFIM for different bond dimensions  $(D, \chi)$  compared to the exact (Lanczos) result (red dashed line). As in the three dimensional case, the relative error of the energy density is the smallest deep in the ferromagnetic phase at small field and is also small deep in the polarized phase. In the critical regime (again shifted slightly to lower field strength compared to the thermodynamic limit (gray dashed) due to open boundaries), there is a peak in the relative error, which decreases systematically with increasing  $D$  and  $\chi$ .

In the bottom panel we observe that only the magnetization-curves of  $(4, 16)$  and  $(5, 20)$  closely match the exact curve in the critical region, indicating that large  $D$  and  $\chi$  are necessary for accurate  $\text{TEBD}^2$ -simulation in this regime. Since the qualitative features of the results of the two dimensional isoTNS simulation precisely matches the case of three dimensions presented here, this is a strong indication that in the critical region, larger  $(D, \chi)$  is needed to faithfully capture the state in three dimensions.

#### IV. CONCLUSION

We have introduced a method for the simulation of three dimensional quantum lattice models using a representation of the wavefunction as three dimensional isometric tensor network states (isoTNS). Generalizing the method for two dimensions presented in Ref. [13] we introduced a tetrahedral splitting of tensors such that time evolving block decimation can be carried out in cubic three dimensional networks in a way that respects the isometric structure and moves the orthogonality center throughout the lattice, an algorithm which we call  $\text{TEBD}^3$ . We expect that our generalization can straightforwardly be used also for higher dimensional hypercubic lattices.

Our systematic benchmark for the 3D transverse field Ising model in the full range of transverse fields across the critical point reveals that our method yields accurate results, and that the systematic error incurring from finite bond dimensions can be controlled systematically by increasing first the embedded tree tensor network bond dimension  $\chi$  and then the PEPS bond dimension  $D$ . This behavior is identical to what is observed in two dimensional isoTNS. The regime close to the critical point is particularly challenging and requires larger bond dimensions, beyond the capacity of our computers for large systems.

While imaginary time evolution using  $\text{TEBD}^3$  is arguably the simplest method for finding the groundstate of a quantum many-body system, it is known even in one dimension that it is not optimal and that local variational energy minimization (e.g. DMRG in 1D) is far more efficient. We expect a similar behavior for isoTNS in higher dimensions and it is possible that our results can be further improved by the formulation of a DMRG

analog for three dimensional isometric tensor networks, a direction which we leave for future study.

#### V. ACKNOWLEDGMENTS

We acknowledge financial support from the Deutsche Forschungsgemeinschaft through SFB 1143 (project-id 247310070).

#### VI. APPENDIX

##### A. Minima in $d\tau$ space

As noted in [13], the error due to the multitude of truncated SVDs and the error due to the trotterization conspire in  $\text{TEBD}^2$  to yield an energy-minimum in  $d\tau$ -space, as can be seen in Fig. 4 of [13]. In Fig. 16 we see that the same effect is observed in  $\text{TEBD}^3$ , where in the top panel we consider the relative energy error of various isoTNS configurations  $(D, \chi)$  on a  $3 \times 3 \times 3$  system across a range of  $d\tau$ . In the bottom panel we have a similar plot but now for various system sizes and a single  $(D, \chi)$ .

##### B. Sequential bias

The sequential nature of a single  $\text{TEBD}^2$ - or  $\text{TEBD}^3$ -iteration, owed to sequentially moving the orthogonality center across all sites, can be expected to introduce a bias when measuring observables. To understand this we start with  $\text{TEBD}^2$ , for which we label the corners of a  $5 \times 5$  system as in the top panel of Fig. 17.

Now, we know from Fig. 6 that in e.g. the second half of a  $\text{TEBD}^2$ -iteration the labeled sites get updated in the sequence  $1 \rightarrow 2 \rightarrow 3 \rightarrow 4$ . As a result we have that upon finishing the final iteration of our  $\text{TEBD}^2$ -optimization we end up with a delay in gate-application between these sites, with site 4 being updated most recently and site 1 longest ago. This likely induces bias, since we compute e.g. the single-body expectation values  $\langle \sigma_i^x \rangle$  only after completing the final iteration of  $\text{TEBD}^2$ .

Specifically, already when the final  $\text{TEBD}^2$ -iteration has finished there is a discrepancy in information-loss between the various sites, since the truncated SVDs which are used to move the orthogonality center in principle induce a loss of information (which can be controlled in principle by increasing  $(D, \chi)$ ). Then when we calculate  $\langle \sigma_i^x \rangle$  for all sites we get a similar effect, since in essence the orthogonality center has to be moved to each site starting from the same corner-site, so that some computations require more SVDs than others.

These two biases likely add instead of cancel, since after evolving the columns in the top panel of Fig. 17 we rotate the lattice counterclockwise by 90 degrees so that the orthogonality center is located in the upper-left corner. As a result we find that site 3, which was

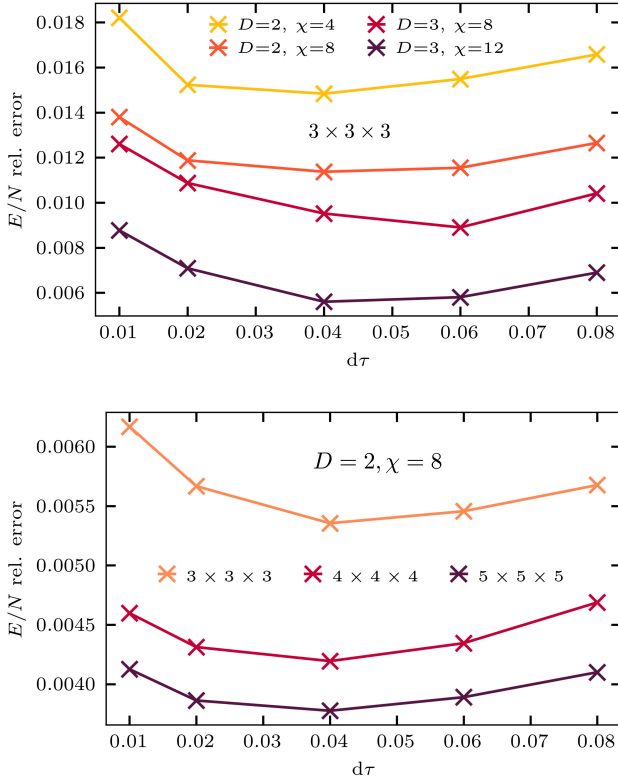


FIG. 16. **Top:** The  $d\tau$ -dependency of the relative error in  $E/N$  for various  $(D, \chi)$ , for the  $3 \times 3 \times 3$  TFIM with OBC and  $h = 4.5$ . We observe a minimum in all cases. **Bottom:** The  $d\tau$ -dependency of the relative error in  $E/N$  for various system sizes at  $h = 2.5$  with  $(D, \chi) = (2, 8)$ , again exhibiting a minimum in all cases.

updated relatively recently, requires no extra truncated SVDs to compute  $\langle \sigma_i^x \rangle$ , whereas site 2, which was updated much further back, requires the maximum amount of extra SVDs. Hence we expect that the interplay between these two biases results in a net site-dependent bias. This could be particularly relevant for large system sizes, since the amount of truncated SVDs necessary to reach the final site is at least linear in system size.

To investigate this prediction numerically we consider  $\langle \sigma_i^x \rangle$  for various sites, organized into the equivalence classes of the lattice symmetry group  $G$  of our  $5 \times 5$  cluster. In the top panel of Fig. 17 we have colored most of the classes, namely by the center site (purple), the four corner sites (red), the four edge sites (orange), and the four edge sites of the  $3 \times 3$  central subset of the lattice (yellow) labeled "bulk". Since in the ferromagnetic 2D TFIM no lattice symmetry breaking is expected, the exact groundstate should inherit the lattice symmetry. Therefore, an exact representation in terms of isoTNS requires that upon convergence  $\langle \sigma_i^x \rangle$  should be identical for all sites  $i$  in a class.

However, since we proceed sequentially through our

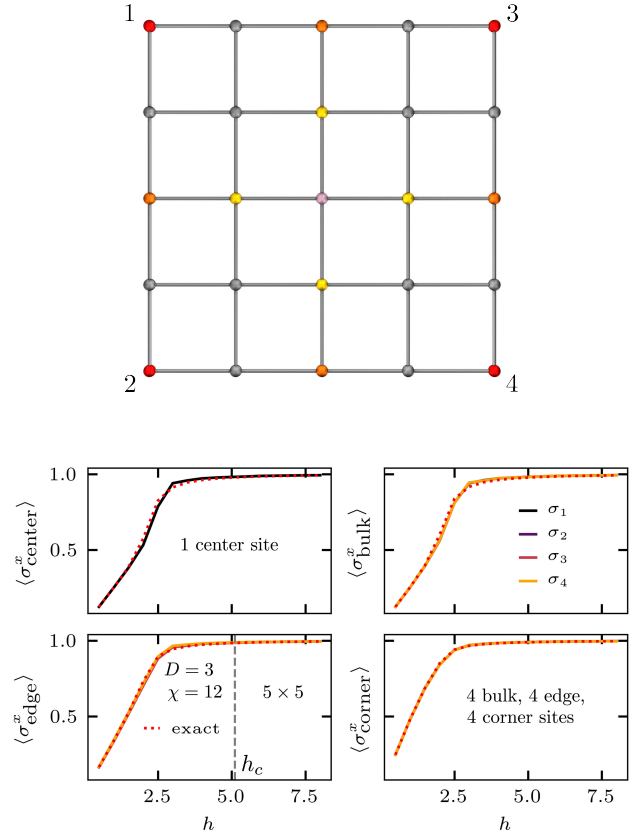


FIG. 17. **Top:** Equivalent sites in the  $5 \times 5$  square lattice with OBC. The center site is shown in purple, the corner sites in red, the edge sites in orange, and the "bulk" sites in yellow. **Bottom:** The local  $x$  magnetization  $\langle \sigma_i^x \rangle$  as a function of field strength  $h$  for the  $5 \times 5$  TFIM. We have a subplot for each equivalence class, containing one curve for each site in the class. The exact result is shown as a red dashed line.

isoTNS, different equivalent sites are not treated on equal footing, thereby likely resulting in a spectrum of  $\langle \sigma_i^x \rangle$  in each group. In the bottom panels of Fig. 17 we show four plots with in each plot the relative energy error across a range of field strength for each site in a class. The red dashed curve corresponds to the exact data and the solid lines to data generated with a  $(3, 12)$  isoTNS.

Looking at the curves within the corner class we see that the magnetization is uniform over all sites and agrees very well with the exact value for all  $h$ . Going to the edge class we start seeing a slight gradation in the magnetization of different sites and slightly lower accuracy in the critical region. For the bulk class we see very little gradation but a further decrease in accuracy for the critical region. Finally we see in the top left panel that the center site has the worst accuracy of all, with visible deviations from the exact curve at various  $h$  surrounding  $h_c$ . From these four panels we see that the accuracy of a site's  $x$  magnetization increases with its amount of bonds, i.e. it is more accurate for the corners, with only 3 bonds, than

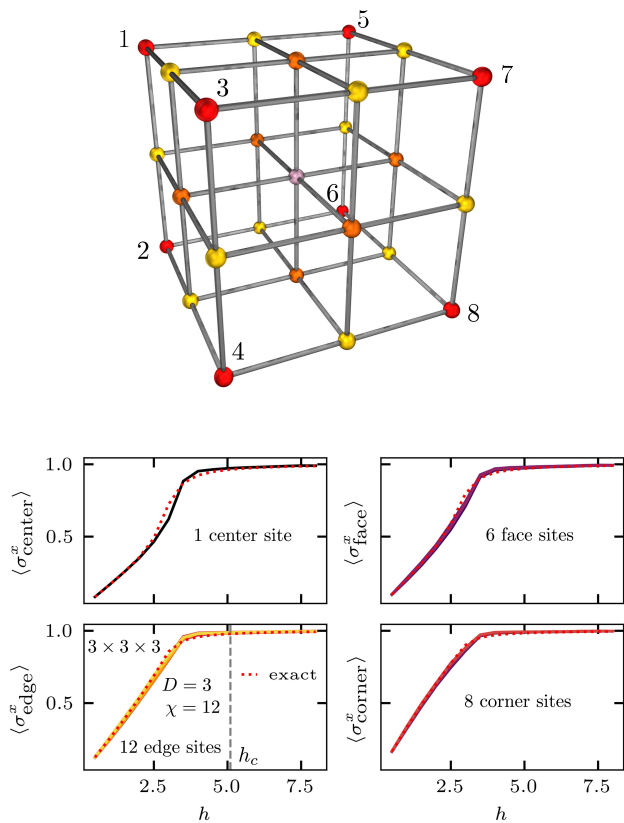


FIG. 18. **Top:** Equivalent sites in the  $3 \times 3 \times 3$  cubic lattice with OBC. The center site is shown in purple, the corner sites in red, the edge sites in yellow, and the face sites in orange. **Bottom:** The local  $x$  magnetization  $\langle \sigma_i^x \rangle$  as a function of field strength  $h$  for the  $3 \times 3 \times 3$  TFIM. We have a subplot for each equivalence class, containing one curve for each site in the class. The exact result is shown as a red dashed line.

for the center, with 6 bonds.

By adding all the curves in these plots we get the (3,12)-curve in the total  $x$ -magnetization plot from the lower panel in Fig. 15. Now we have an idea about the separate accuracies of its constituents, as well as the effect of the sequential bias.

Analogously, we consider the sequential bias in TEBD<sup>3</sup>, for which we repeat the above procedure, now for a  $3 \times 3 \times 3$  cluster. We again start by dividing the cluster into its equivalence classes, as illustrated in the top panel of Fig. 18, which consist of the center site (purple), the six face sites (orange), the twelve edge sites (yellow), and the eight corner sites (red).

In the bottom panels of Fig. 18 we plot the local  $x$  magnetization curves for all the sites in each class, for a 3D isoTNS with (3,12). As opposed to the results for TEBD<sup>2</sup> in Fig. 17 we see in the bottom panels of Fig. 17 that there now is gradation in every class with multiple members. Moreover, similar to TEBD<sup>2</sup> we see that the accuracy of a site's  $x$  magnetization decreases with its amount of bonds, with the corner class being accurately simulated across all  $h$  and the center site showing significant deviations in the critical region. These results indicate that the visible discrepancy of the (3,12)-curve around  $h_c$  in the bottom panel of Fig. 12 is largely due to the center and face sites.

The larger spread in single-site  $x$  magnetization relative to TEBD<sup>2</sup> can probably be partially attributed to (3,12) being more accurate in TEBD<sup>2</sup> than in TEBD<sup>3</sup> for roughly equal system sizes, as can be seen from Figs. 12 and 15.

This property is in itself likely caused by the difference in complexity of the square and cubic TFIM, which can be attributed to the difference in dimensionality.

- 
- [1] M. B. Hastings, “An area law for one-dimensional quantum systems,” *Journal of Statistical Mechanics: Theory and Experiment* **2007**, P08024–P08024 (2007).
  - [2] M. B. Hastings, “Locality in Quantum and Markov Dynamics on Lattices and Networks,” *Physical Review Letters* **93**, 140402 (2004).
  - [3] J. Eisert, M. Cramer, and M. B. Plenio, “Colloquium: Area laws for the entanglement entropy,” *Reviews of Modern Physics* **82**, 277–306 (2010).
  - [4] U. Schollwoeck, “The density-matrix renormalization group in the age of matrix product states,” *Annals of Physics* **326**, 96192 (2011).
  - [5] S. R. White, “Density matrix formulation for quantum renormalization groups,” *Phys. Rev. Lett.* **69**, 2863–2866 (1992).
  - [6] F. Verstraete and J. I. Cirac, “Renormalization algorithms for quantum-many body systems in two and higher dimensions,” (2004), [arXiv:cond-mat/0407066](https://arxiv.org/abs/cond-mat/0407066).
  - [7] N. Schuch, M. M. Wolf, F. Verstraete, and J. I. Cirac, “Computational complexity of projected entangled pair states,” *Phys. Rev. Lett.* **98**, 140506 (2007).
  - [8] M. Lubasch, J. I. Cirac, and M.-C. Bañuls, “Unifying projected entangled pair state contractions,” *New Journal of Physics* **16**, 033014 (2014).
  - [9] F. Verstraete, V. Murg, and J. I. Cirac, “Matrix product states, projected entangled pair states, and variational renormalization group methods for quantum spin systems,” *Advances in Physics* **57**, 143–224 (2008).
  - [10] M. Lubasch, J. I. Cirac, and M.-C. Bañuls, “Algorithms for finite projected entangled pair states,” *Phys. Rev. B* **90**, 064425 (2014).
  - [11] G. Vidal, “Efficient Classical Simulation of Slightly Entangled Quantum Computations,” *Physical Review Letters* **91**, 147902 (2003).
  - [12] S. Paeckel, T. Khler, A. Swoboda, S. R. Manmana, U. Schollwoeck, and C. Hubig, “Time-evolution methods for matrix-product states,” *Annals of Physics* **411**, 167998 (2019).
  - [13] M. P. Zaletel and F. Pollmann, “Isometric tensor network states in two dimensions,” (2019), [arXiv:1902.05100](https://arxiv.org/abs/1902.05100).

- [14] M. Zaletel, “Isometric Tensor Network States in Two Dimensions,” (2019), talk at Perimeter Institute.
- [15] R. Haghshenas, M. J. O’Rourke, and G. K.-L. Chan, “Conversion of projected entangled pair states into a canonical form,” *Phys. Rev. B* **100**, 054404 (2019).
- [16] K. Hyatt and E. M. Stoudenmire, “DMRG Approach to Optimizing Two-Dimensional Tensor Networks,” (2019), [arXiv:1908.08833](https://arxiv.org/abs/1908.08833).
- [17] T. Soejima, K. Siva, N. Bultinck, S. Chatterjee, F. Pollmann, and M. P. Zaletel, “Isometric tensor network representation of string-net liquids,” (2019), [arXiv:1908.07545](https://arxiv.org/abs/1908.07545).
- [18] P. Teng, “Generalization of the tensor renormalization group approach to 3-d or higher dimensions,” *Physica A: Statistical Mechanics and its Applications* **472**, 117 – 135 (2017).
- [19] A. García-Sáez and J. I. Latorre, “Renormalization group contraction of tensor networks in three dimensions,” *Phys. Rev. B* **87**, 085130 (2013).
- [20] S. Anders, M. B. Plenio, W. Dür, F. Verstraete, and H.-J. Briegel, “Ground-state approximation for strongly interacting spin systems in arbitrary spatial dimension,” *Phys. Rev. Lett.* **97**, 107206 (2006).
- [21] A. Sfondrini, J. Cerrillo, N. Schuch, and J. I. Cirac, “Simulating two- and three-dimensional frustrated quantum systems with string-bond states,” *Phys. Rev. B* **81**, 214426 (2010).
- [22] M. Schmitt and M. Heyl, “Quantum dynamics in transverse-field Ising models from classical networks,” *SciPost Phys.* **4**, 013 (2018).
- [23] F. Verstraete, M. M. Wolf, D. Perez-Garcia, and J. I. Cirac, “Criticality, the area law, and the computational power of projected entangled pair states,” *Phys. Rev. Lett.* **96**, 220601 (2006).
- [24] Y.-Y. Shi, L.-M. Duan, and G. Vidal, “Classical simulation of quantum many-body systems with a tree tensor network,” *Phys. Rev. A* **74**, 022320 (2006).
- [25] F. A. Y. N. Schroeder, D. H. P. Turban, A. J. Musser, N. D. M. Hine, and A. W. Chin, “Tensor network simulation of multi-environmental open quantum dynamics via machine learning and entanglement renormalisation,” *Nature Communications* **10** (2019), 10.1038/s41467-019-09039-7.
- [26] J. Hauschild, E. Leviatan, J. H. Bardarson, E. Altman, M. P. Zaletel, and F. Pollmann, “Finding purifications with minimal entanglement,” *Phys. Rev. B* **98**, 235163 (2018).
- [27] M. P. Holmes, J. Isbell, C. Lee, and A. G. Gray, “QUIC-SVD: Fast SVD Using Cosine Trees,” in *Advances in Neural Information Processing Systems 21*, edited by D. Koller, D. Schuurmans, Y. Bengio, and L. Bottou (Curran Associates, Inc., 2009) pp. 673–680.
- [28] D. J. Luitz, F. Alet, and N. Laflorencie, “Universal behavior beyond multifractality in quantum many-body systems,” *Phys. Rev. Lett.* **112**, 057203 (2014).
- [29] H. W. J. Blöte and Y. Deng, “Cluster monte carlo simulation of the transverse ising model,” *Phys. Rev. E* **66**, 066110 (2002).
- [30] A. W. Sandvik and J. Kurkijärvi, “Quantum monte carlo simulation method for spin systems,” *Phys. Rev. B* **43**, 5950–5961 (1991).
- [31] A. W. Sandvik, “A generalization of handscomb’s quantum monte carlo scheme-application to the 1d hubbard model,” *Journal of Physics A: Mathematical and General* **25**, 3667–3682 (1992).
- [32] B. Bauer, L. D. Carr, H. G. Evertz, A. Feiguin, J. Freire, S. Fuchs, L. Gamper, J. Gukelberger, E. Gull, S. Guertler, A. Hehn, R. Igarashi, S. V. Isakov, D. Koop, P. N. Ma, P. Mates, H. Matsuo, O. Parcollet, G. Pawłowski, J. D. Picon, L. Pollet, E. Santos, V. W. Scarola, U. Schollwck, C. Silva, B. Surer, S. Todo, S. Trebst, M. Troyer, M. L. Wall, P. Werner, and S. Wessel, “The ALPS project release 2.0: open source software for strongly correlated systems,” *Journal of Statistical Mechanics: Theory and Experiment* **2011**, P05001 (2011).
- [33] A. F. Albuquerque, F. Alet, P. Corboz, P. Dayal, A. Feiguin, S. Fuchs, L. Gamper, E. Gull, S. Grtler, A. Honecker, R. Igarashi, M. Krner, A. Kozhevnikov, A. Luchli, S. R. Manmana, M. Matsumoto, I. P. McCulloch, F. Michel, R. M. Noack, G. Pawowski, L. Pollet, T. Pruschke, U. Schollwck, S. Todo, S. Treb, M. Troyer, P. Werner, and S. Wessel, “The alps project release 1.3: Open-source software for strongly correlated systems,” *Journal of Magnetism and Magnetic Materials* **310**, 11871193 (2007), proceedings of the 17th International Conference on Magnetism.